On the use of block-effective macrodispersion for numerical simulations of transport in heterogeneous formations

Yoram Rubin

Department of Civil and Environmental Engineering, University of California, Berkeley, California, USA

Alberto Bellin

Dipartimento di Ingegneria Civile ed Ambientale, Università di Trento, Trento, Italy

Alison E. Lawrence

Department of Civil and Environmental Engineering, University of California, Berkeley, California, USA

Received 17 September 2002; revised 14 May 2003; accepted 22 May 2003; published 11 September 2003.

[1] The fundamental question we consider in this paper is how to allow flexibility in numerical grid design without discounting the dispersive action of the unmodeled variability. In doing that, we wish to preserve the interplay between all relevant length scales: those relevant to the spatial variability as well as those created by design. In this study we extend and test the concept of block-scale macrodispersion introduced by *Rubin et al.* [1999] for modeling unresolved hydraulic property variations at scales smaller than the numerical grid blocks. We present closed-form analytical results for the block-scale macrodispersion and test them numerically. Closed-form analytical results are presented for the large-time aymptotic limits, and it is shown that these limits are attained very fast. The conditions of applicability are investigated, and we show that ergodicity with regard to block-scale heterogeneity is attained surprisingly fast. *INDEX TERMS:* 1832 Hydrology: Groundwater transport; 1829 Hydrology: Groundwater hydrology

Citation: Rubin, Y., A. Bellin, and A. E. Lawrence, On the use of block-effective macrodispersion for numerical simulations of transport in heterogeneous formations, *Water Resour. Res.*, *39*(9), 1242, doi:10.1029/2002WR001727, 2003.

1. Introduction

[2] Modeling of contaminant transport in the subsurface requires consideration of many length scales, as illustrated in Figure 1. First let us define the space random function (SRF) Y, representing the spatial variability of the log conductivity. The integral scale of Y, $I_{Y,i}$, with the subscript i denoting the Cartesian direction, is the distance over which Y is strongly correlated. The size of the plume, $l_i(t)$, must also be considered. Three additional length scales to consider include the size of the numerical grid blocks, Δ_i; the size of the domain modeled, L_i; and finally, λ_i, the dimension of the homogenized regions (note that in many applications, $\lambda_i = \Delta_i$ is taken, but for greater flexibility we define homogenized regions of scales λ_i possibly larger than Δ_i). These length scales are obviously important in any numerical modeling exercise, but in particular when considering the variability that is not captured over homogenized regions of the simulated domain vis-a-vis the variability that acts on solute bodies by way of advection and dispersion. The effect of these length scales on transport can be conveniently analyzed in Fourier space, whereby the spatial variability can be described through a series of wave number vectors, $\boldsymbol{k}$.

[3] With the aid of Nyquist's theorem [*Bras and Rodriguez-Iturbe*, 1985] we can identify λ_i and $l_i(t)$ as important cut-offs. First, $|k_i| \leq \pi/\lambda_i$ defines the variability that is captured over the grid, while $|k_i| > \pi/\lambda_i$ is the variability which is wiped out due to homogenization, and which must be modelled indirectly, for example using dispersion coefficients. Then, there is the set of cut-offs $\pi/l_i(t)$, corresponding to the plume's scales. Here, $|k_i| > \pi/l_i(t)$ defines the variability that disperses the solutes. The order relationship between $l_i(t)$ and λ_i is important when modeling the effects of the wiped out variability. This point is demonstrated in Figure 2.

[4] In this paper, we review the concept of block-effective macrodispersion presented by *Rubin et al.* [1999] with an application to the case of a hydraulic conductivity field described by a Gaussian spatial covariance model. We investigate the case of a nonergodic plume and determine the conditions required for applicability of the theory. Next, we suggest a quick way to obtain the block-effective macrodispersion tensor and finally, we test numerically the proposed methodology.

2. Block-Effective Macrodispersion Tensor

[5] Let us consider a stationary log-hydraulic conductivity field with mean m_Y and variance σ_Y^2. Following *Rubin et al.* [1999], we split Y into three components:

$$Y(\mathbf{x}) = m_Y + \overline{Y}(\mathbf{x}) + \widetilde{Y}(\mathbf{x}), \tag{1}$$

where $\overline{Y}$ and $\widetilde{Y}$ are the zero-mean large- and small-scale fluctuations, respectively. $\overline{Y}$ represents the variability that is

0043-1397/03/2002WR001727

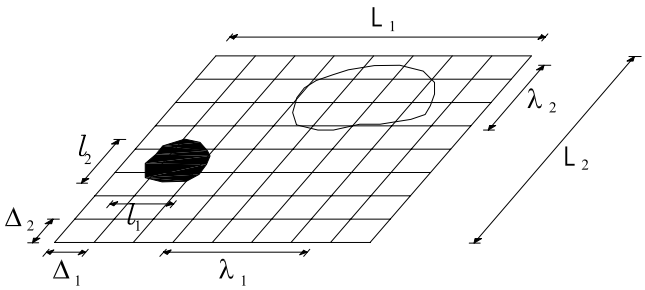

Figure 1. Illustration of relevant length scales in a two-dimensional domain: l_i is plume size, λ_i is dimensions of homogenized regions (when larger than Δ_i), L_i is domain size, Δ_i is grid block size.

captured by the grid, and $\widetilde{Y}$ represents subgrid-scale variability that is lost due to homogenization. Subsequently we refer to $\overline{Y}$ as large-scale variability and $\widetilde{Y}$ as the small-scale variability. From Nyquist's theorem, $\overline{Y}$ is characterized by the following covariance in Fourier space:

$$\widehat{C}_{\overline{Y}}(\boldsymbol{k}) = \begin{cases} \widehat{C}_Y(\boldsymbol{k}) & \text{for} \quad |k_i| \le \frac{\pi}{\lambda_i}, \quad i = 1, ..., m \\ 0 & \text{otherwise} \end{cases}, \tag{2}$$

In (2), λ_i, $i = 1,\ldots,m$, are the dimensions of homogenized regions, and $\widehat{C}_Y$ is the Fourier transform of the covariance function of Y, [*Rubin*, 2003, chap. 3]. $\boldsymbol{k}$ is the vector of wave numbers in Fourier space, and m is the number of space dimensions considered in the problem. $\widehat{C}_Y(\boldsymbol{k})$ is related to the spatial covariance $C_Y(\boldsymbol{r})$ through [*Rubin*, 2003, equation 2.44]:

$$\widehat{C}_Y(\boldsymbol{k}) = \frac{1}{(2\pi)^{m/2}} \int_{-\infty}^{\infty} \ldots \int_{-\infty}^{\infty} C_Y(r)\, e^{\imath\, \boldsymbol{k} \cdot r} d^m r \tag{3}$$

where $d^m \boldsymbol{r} = dr_1, \ldots, dr_m$, and $\imath = \sqrt{-1}$ is the imaginary unit.

[6] Following (2), $\widehat{C}_Y$ can be decomposed into two separate components, representing the large-scale and small-scale variability, as follows:

$$\widehat{C}_Y(\boldsymbol{k}) = \widehat{C}_{\overline{Y}}(k) + \widehat{C}_{\widetilde{Y}}(\boldsymbol{k}) = [1 - F(\boldsymbol{k})]\, \widehat{C}_Y(\boldsymbol{k}) + F(\boldsymbol{k})\, \widehat{C}_Y(\boldsymbol{k}). \tag{4}$$

In (4), $F(\boldsymbol{k})$ is the high-pass filter:

$$F(\boldsymbol{k}) = \begin{cases} 0 & \text{for} \quad |k_i| \le \frac{\pi}{\lambda_i}, i = 1, ..., m \\ 1 & \text{otherwise} \end{cases}. \tag{5}$$

[7] According to (4) the variances of $\widetilde{Y}$ and $\overline{Y}$ satisfy:

$$\sigma_Y^2 = \sigma_{\overline{Y}}^2 + \sigma_{\widetilde{Y}}^2, \tag{6}$$

where $\sigma_{\overline{Y}}^2$ and $\sigma_{\widetilde{Y}}^2$ are the variances of $\overline{Y}$ and $\widetilde{Y}$, respectively. Although both $\sigma_{\overline{Y}}^2$ and $\sigma_{\widetilde{Y}}^2$ are smaller than σ_Y^2, no order relationship exists between $\overline{Y}$ and $\widetilde{Y}$, and both are of the order of the standard deviation σ_Y [*Rubin et al.*, 1999]. The covariance of $\overline{Y}$ is given by:

$$C_{\overline{Y}}(r) = \frac{1}{(2\pi)^{m/2}} \int_{-\pi/\lambda_1}^{\pi/\lambda_1} \ldots \int_{-\pi/\lambda_m}^{\pi/\lambda_m} \widehat{C}_Y(\boldsymbol{k})\, e^{-\imath\, \boldsymbol{k} \cdot r}\, d^m \boldsymbol{k}, \tag{7}$$

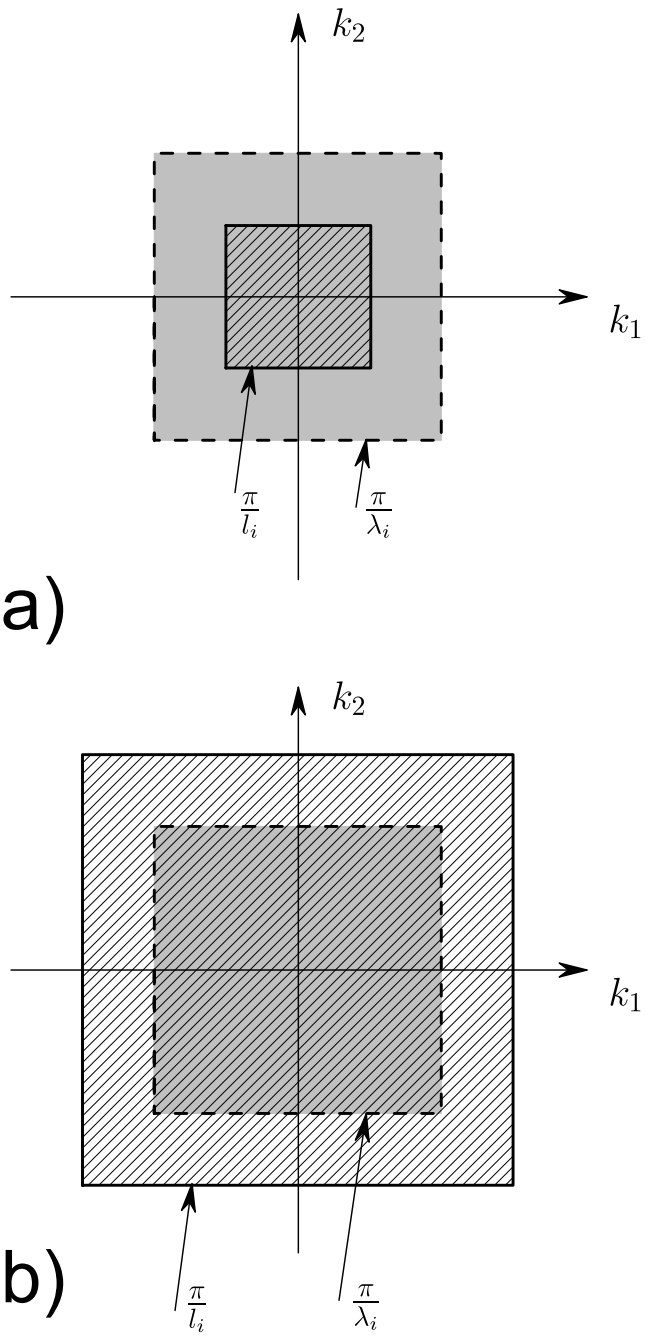

Figure 2. This figure represents schematically the interplay between l_i and λ_i in two dimensions. In both diagrams the hatched area (surrounded by solid line) represents the subdomain of $\boldsymbol{k}$ not affecting mixing, while the subdomain not shaded contains the wave numbers that cannot be simulated over the grid: (a) this is the case of a large plume $l_i > \lambda_i$. Here the unmodeled spatial variability is defined by λ_i and does not depend on l_i. The wave numbers contained in the hatched, shaded area will be filtered out by the plume scales, and no special action is needed. (b) This is the case of a small plume $l_i < \lambda_i$. Here the wave numbers that affect mixing are defined by l_i, not λ_i. As l_i increase, we will observe a transition from the state described in Figure 2b to the state described in Figure 2a.

and the variance of $\overline{Y}$ is obtained by setting $\boldsymbol{r} = 0$ in (7):

$$\sigma^2_{\overline{Y}} = \frac{1}{(2\pi)^{m/2}} \int_{-\pi/\lambda_1}^{\pi/\lambda_1} \ldots \int_{-\pi/\lambda_m}^{\pi/\lambda_m} \widehat{C}_Y(\boldsymbol{k})\, d^m\boldsymbol{k} \quad . \tag{8}$$

[8] With the variability $C_{\overline{Y}}(\boldsymbol{k})$ captured by the grid, we are left with the challenge of modeling the effects of the small-scale variability, $C_{\widetilde{Y}}(\boldsymbol{k})$. We propose to do that using the block-effective dispersion tensor. This concept calls for augmenting the dispersive action of the large-scale variability with tensors representing the effects of the small-scale variability. In doing that the distribution of the concentration is characterized by a support-scale of size λ, as a result of the lack of resolution in describing the detailed actual concentration distribution at scales smaller than λ (this issue is also discussed by *Wang and Kitanidis* [1999]).

[9] For a complete perspective, let us consider the case where none of the variability is captured over the grid, and its effects are modeled entirely through a macrodispersion tensor. The tensor in this case assumes the form [*Dagan*, 1989]:

$$D^*_{ij}(t) = \frac{U^2}{(2\pi)^{m/2}} \int_0^t \left[\int_{-\infty}^{\infty} \ldots \int_{-\infty}^{\infty} e^{-\imath\, k_1 U \tau} \cdot \left(\delta_{i1} - \frac{k_1 k_i}{k^2}\right)\left(\delta_{j1} - \frac{k_1 k_j}{k^2}\right) \widehat{C}_Y(\boldsymbol{k})\, dk_1 \ldots dk_m \right] d\tau, \quad i,j = 1, \ldots, m \tag{9}$$

where the ensemble average of the velocity, U, is in the x_1 direction, and δ is the Kronecker delta. Note that (9) is limited to small variance of the log conductivity, i.e., $\sigma^2_Y < 1$. *Rubin et al.* [1999] (see equation (38)) conclude that the dispersion tensor representing the effects of the small-scale variability, or in other words, the variability which is wiped out, is given by:

$$\widetilde{D}^{ens}_{ij}(t) = D^*_{ij}(t) - \frac{U^2}{(2\pi)^{m/2}} \int_0^t \left[\int_{-\frac{\pi}{\lambda_1}}^{\frac{\pi}{\lambda_1}} \ldots \int_{-\frac{\pi}{\lambda_m}}^{\frac{\pi}{\lambda_m}} e^{-\imath\, k_1 U \tau} \cdot \left(\delta_{i1} - \frac{k_i k_1}{k^2}\right)\left(\delta_{j1} - \frac{k_j k_1}{k^2}\right) \widehat{C}_Y(\boldsymbol{k})\, dk_1 \ldots dk_m \right] d\tau. \tag{10}$$

This derivation, similar to (9), is limited to $\sigma^2_Y < 1$.

[10] In (10), the superscript "ens" intends to emphasize that this tensor is applicable to solute plumes which are ergodic with respect to the integral scale of the small-scale (wiped out) variability. This is in line with the discussion by *Dagan* [1991]. The idea is that nonergodic plumes are those which are not too much larger than the integral scale of the wiped out variability. As such, the wiped out spatial variability affects the displacement of its centroid and cannot be modeled only as a dispersive effect. We shall revisit this topic in Section 3.

[11] *Rubin et al.* [1999] applied their results to the case of an exponential covariance. Let us expand their work for the case of a Gaussian covariance. The power spectrum of the Gaussian covariance model can be determined by taking the Fourier transform of the Gaussian covariance model, which, in two dimensions, is [*Rubin*, 2003, chap. 3]

$$C_Y(r_1, r_2) = \sigma^2_Y \exp\left\{ -\frac{\pi}{4}\left[\left(\frac{r_1}{I_{Y,1}}\right)^2 + \left(\frac{r_2}{I_{Y,2}}\right)^2 \right] \right\}, \tag{11}$$

where r is the separation distance, leading to

$$\widehat{C}_Y(k_1, k_2) = \frac{2\sigma^2_Y I_{Y,1}\, I_{Y,2}}{\pi} \exp\left[-\frac{1}{\pi}(k_1^2 I^2_{Y,1} + k_2^2 I^2_{Y,2}) \right], \tag{12}$$

where $I_{Y,1}$ and $I_{Y,2}$ are the longitudinal and transverse log transmissivity integral scales, respectively. Substituting (12) into (10) and solving for $i = j = 1$ as well as $i = j = 2$, we obtain the longitudinal and transverse components of the block-effective macrodispersion tensor for the Gaussian covariance model as follows:

$$\widetilde{D}^{ens}_{11}(t) = D^*_{11}(t) - \frac{4\sigma^2_Y U I_{Y,1} I_{Y,2}}{\pi^2} \int_0^{\frac{\pi}{\lambda_1}} \frac{\sin(k_1 U t)}{k_1} e^{\frac{-I^2_{Y,1}k_1^2}{\pi}} \cdot \left[\int_0^{\frac{\pi}{\lambda_2}} \left(1 - \frac{k_1^2}{k_1^2 + k_2^2}\right)^2 e^{\frac{-I^2_{Y,2}k_2^2}{\pi}} dk_2 \right] dk_1, \tag{13}$$

and

$$\widetilde{D}^{ens}_{22}(t) = D^*_{22}(t) - \frac{4\sigma^2_Y U I_{Y,1} I_{Y,2}}{\pi^2} \int_0^{\frac{\pi}{\lambda_1}} k_1 \sin(k_1 U t) e^{\frac{-I^2_{Y,1}k_1^2}{\pi}} \cdot \left[\int_0^{\frac{\pi}{\lambda_2}} \frac{k_2^2}{(k_1^2 + k_2^2)^2} e^{\frac{-I^2_{Y,2}k_2^2}{\pi}} dk_2 \right] dk_1. \tag{14}$$

[12] $D^*_{11}(t)$ and $D^*_{22}(t)$ in (13) and (14) are for the Gaussian covariance case and are given by

$$D^*_{11}(t) = \frac{4\sigma^2_Y U I_{Y,1} I_{Y,2}}{\pi^2} \int_0^{\infty} \frac{\sin(k_1 U t)}{k_1} e^{\frac{-I^2_{Y,1}k_1^2}{\pi}} \cdot \left[\int_0^{\infty} \left(1 - \frac{k_1^2}{k_1^2 + k_2^2}\right)^2 e^{\frac{-I^2_{Y,2}k_2^2}{\pi}} dk_2 \right] dk_1, \tag{15}$$

$$D^*_{22}(t) = \frac{4\sigma^2_Y U I_{Y,1} I_{Y,2}}{\pi^2} \int_0^{\infty} k_1 \sin(k_1 U t) e^{\frac{-I^2_{Y,1}k_1^2}{\pi}} \cdot \left[\int_0^{\infty} \frac{k_2^2}{(k_1^2 + k_2^2)^2} e^{\frac{-I^2_{Y,2}k_2^2}{\pi}} dk_2 \right] dk_1. \tag{16}$$

In the isotropic case, $I_{Y,1} = I_{Y,2} = I_Y$, closed form results for (15) and (16) are given by:

$$D^*_{11}(t) = \frac{U I_Y}{\pi^2\, t'^3} \cdot \left[4 - 3\,\pi\, t'^2 + 2\left(-2 + \pi\, t'^2\right).\exp\left(-\frac{\pi\, t'^2}{4}\right) + \pi^2\, t'^3\, Erf\left(\frac{\sqrt{\pi}\, t'}{2}\right) \right], \tag{17}$$

and

$$D^*_{22}(t) = \frac{U I_Y}{\pi^2\, t'^3} \left[-4 + 4\, \exp\left(-\frac{\pi\, t'^2}{4}\right) + \pi\, t'^2 \right], \tag{18}$$

where $t' = t\, U/I_Y$ is dimensionless time.

[13] Figure 3 depicts the longitudinal block-effective dispersion coefficient ($\widetilde{D}^{ens}_{11}$) as a function of travel time, and as a function of λ. The time dependence of these coefficients is a well-documented effect [*Dagan*, 1984; *Rubin*, 2003, chaps. 8 and 10; *Rubin and Bellin*, 1994]. The scale λ plays,

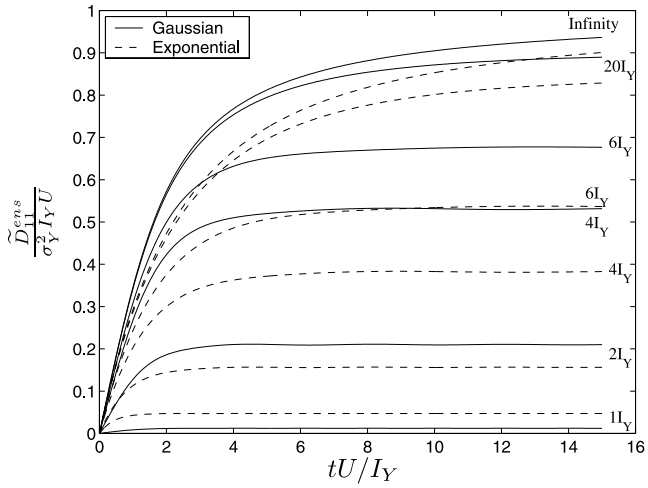

Figure 3. The longitudinal ensemble average block-scale macrodispersion as a function of λ (marked on each curve) and dimensionless travel time with $I_{Y,1} = I_{Y,2} = I_Y$ and $\lambda_1 = \lambda_2 = \lambda$ for a Gaussian covariance model, (13), and an exponential covariance model (equation (42) of *Rubin et al.* [1999]).

as one would expect, a prominent role in determining the magnitude of these coefficients. As λ increases, a larger part of the variability is wiped out, and coefficients increase in magnitude, to compensate for this loss. As λ increases and more variability is wiped out, the integral scale of the wiped out variability increases as well, and with it the time to reach the large time, asymptotic level. However, for λ values that can be expected in applications, which are of the order of I_Y or less, the time to asymptotes is quite short, and the asymptotic limit can be used throughout the simulation. We also note the different patterns of $\widetilde{D}_{11}^{ens}$ imparted by the two types of spatial covariances. This is an outcome of the different distributions of variability between smaller and larger scales which characterize these covariances, as shown in Figure 4.

[14] The large-time asymptotic limit of the longitudinal ensemble average block-scale macrodispersion coefficient is given by

$$\widetilde{D}_{11}^{ens,\infty} = D_{11}^{*,\infty} - U^2 \int_0^\infty C_{\overline{Y}}(U\tau, 0)\, d\tau = \sigma_Y^2 U I_{Y,1} - \sigma_{\overline{Y}}^2 U I_{\overline{Y},1} \tag{19}$$

where

$$I_{\overline{Y},1} = \frac{1}{\sigma_{\overline{Y}}^2} \int_0^\infty C_{\overline{Y}}(r, 0)\, dr \tag{20}$$

is the longitudinal integral scale of $\overline{Y}$. From (19) we note that the asymptotic limit of $\widetilde{D}_{11}^{ens}$ can be easily determined from C_Y, using equations (8) and (20). Closed form expressions for $I_{\overline{Y}}$ and $\sigma_{\overline{Y}}^2$ for both the exponential and Gaussian covariance models are provided in Appendix A, allowing a quick computation of (19). In the case of a two-dimensional isotropic Gaussian covariance,

$$\widetilde{D}_{11}^{ens,\infty} = \sigma_Y^2 I_Y U \left(1 - erf\left[\frac{\sqrt{\pi}}{\lambda}\right]\right) \tag{21}$$

where we assumed $\lambda_1 = \lambda_2 = \lambda$. For $\lambda \to \infty$, i.e., when the homogenized regions are infinitely large, $\widetilde{D}_{11}^{ens,\infty}$ is equal to $\sigma_Y^2 I_Y U$, the well known result for the large-time asymptotic limit of macrodispersion [*Dagan*, 1984] [see also *Rubin*, 2003, chaps. 8 and 10].

3. Applications

[15] $\widetilde{D}_{ij}^{ens}$ are obtained by ensemble averaging, and as such, are applicable for deterministic prediction only at the limit where space and ensemble averaging over Y coincide. A solute body that disperses with $\widetilde{D}_{ij}^{ens}$ must satisfy conditions which are investigated below. Our discussion follows that of *Dagan* [1991] which investigated the limits of applicability of (9). In that work solute bodies that disperse with D_{ij}^* were referred to as ergodic. The notable difference between the work of *Dagan* [1991] and the analysis below is that here we evaluate ergodicity with respect to $\widehat{C}_{\widetilde{Y}}(\boldsymbol{k})$, and not with respect to $\widehat{C}_Y(\boldsymbol{k})$.

[16] Let us consider the case of an instantaneous release of solute with constant concentration, C_0, within the volume, V_0, which extends over the thickness of the aquifer, with A_0, which is centered at the origin, representing the horizontal projection of V_0. The spreading of the resulting plume can be described through its spatial moments

$$R_i(t) = \frac{1}{M_0} \int C(\mathbf{x}, t) x_i d\mathbf{x};$$
$$S_{ij}(t) = \frac{1}{M_0} \int C(\mathbf{x}, t) \left[x_i - R_i(t)\right] \cdot \left[x_j - R_j(t)\right] d\mathbf{x}, \tag{22}$$

where $M_0 = n\, C_0 A_0$ is the total mass of solute released into the aquifer per unit of thickness, R_i, $i = 1,2$ is the i-th component of the trajectory of the plume's centroid $\boldsymbol{R}$, $C(\mathbf{x}, t)$ is the average concentration over the aquifer's thickness, and S_{ij}, $i, j = 1, 2$ are the second-order spatial moments. For a plume of limited size, the moments in (22) are not deterministic, and can only be characterized by their statistical moments. The actual spatial moments are

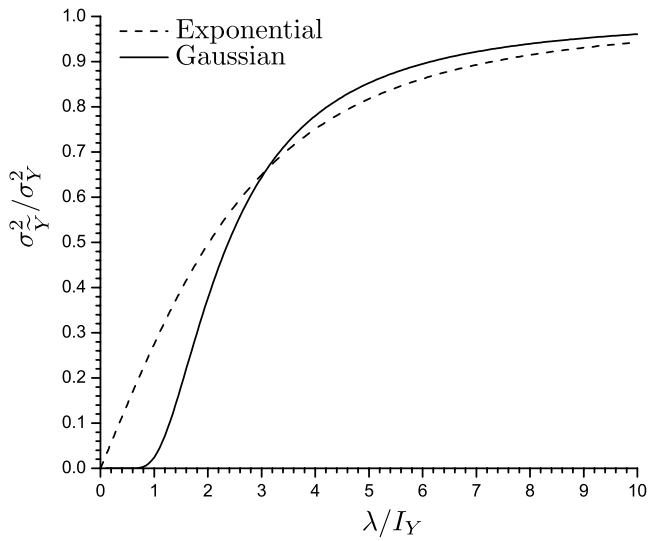

Figure 4. Variance of the small-scale fluctuations of the exponential and Gaussian covariance models with $I_{Y,1} = I_{Y,2} = I_Y$, and $\lambda_1 = \lambda_2 = \lambda$.

expected to differ from their expected values. In the case of uniform in the average flow, the expected value of the centroid's displacement is given by:

$$\langle R_i(t)\rangle = \delta_{i1} Ut \tag{23}$$

while the second moments satisfy [*Kitanidis*, 1988; *Dagan*, 1991]:

$$\langle S_{ij}(t)\rangle = S_{ij}(0) + X_{ij}(t) - R_{ij}(t), \tag{24}$$

where $S_{ij}(0)$ is the second moment of V_0 about its centroid, $X_{ij}(t)$ is the particle displacement variance-covariance tensor, and R_{ij} is the variance-covariance tensor of $\boldsymbol{R}$. Inasmuch as $D^*_{ij} = 1/2\ dX_{ij}(t)/dt$, the plume becomes ergodic when $R_{ij}(t) = 0$, and the variance of $S_{ij}(t)$ is equal to zero [*Rubin*, 2003, sect. 10.3]. At the first-order approximation in σ^2_Y, R_{ij} assumes the following form [*Dagan*, 1991]:

$$R_{ij}(t) = \frac{1}{A_0^2\pi}\int_{A_0}\int_{A_0}\int_{-\infty}^{\infty}\int_{-\infty}^{\infty} \frac{cos[k_1\ (a_1-b_1)+k_2\ (a_2-b_2)][1-cos(k_1Ut)]}{k_1^2} \cdot\left(\delta_{1i}-\frac{k_1k_i}{k^2}\right)\left(\delta_{1j}-\frac{k_1k_j}{k^2}\right)\widehat{C}_Y(k_1,k_2)\ dk_1\ dk_2\ d^2\mathbf{a}\ d^2\mathbf{b}, \tag{25}$$

where $\mathbf{a}=(a_1,a_2)$, $\mathbf{b}=(b_1,b_2)$, and $k=\sqrt{k_1^2+k_2^2}$. Furthermore $X_{ij}(t)$ is given by [*Dagan*, 1989]

$$X_{ij}(t) = \frac{1}{\pi}\int_{-\infty}^{\infty}\frac{1-cos(k_1tU)}{k_1^2}\int_{-\infty}^{\infty}\left(\delta_{1i}-\frac{k_1k_i}{k^2}\right)\left(\delta_{1j}-\frac{k_1k_j}{k^2}\right) \cdot\widehat{C}_Y(k_1,k_2)\ dk_1\ dk_2. \tag{26}$$

[17] Following the same procedure employed by *Dagan* [1991], coupled with (5), a relationship analogous to (24), only applicable to a solute body which disperses due to the action of $\widetilde{Y}$ only, is:

$$\langle\widetilde{S}_{ij}(t)\rangle = \widetilde{X}_{ij}(t) - \widetilde{R}_{ij}(t), \tag{27}$$

where

$$\widetilde{X}_{ij}(t) = X_{ij}(t) - \frac{1}{\pi}\int_{-\frac{\pi}{\lambda_1}}^{\frac{\pi}{\lambda_1}}\frac{1-cos(k_1tU)}{k_1^2} \cdot\int_{-\frac{\pi}{\lambda_2}}^{\frac{\pi}{\lambda_2}}\left(\delta_{1i}-\frac{k_1k_i}{k^2}\right)\left(\delta_{1j}-\frac{k_1k_j}{k^2}\right)\widehat{C}_Y(k_1,k_2)\ dk_1\ dk_2 \tag{28}$$

and

$$\widetilde{R}_{ij}(t) = R_{ij}(t) - \frac{1}{A_0^2\pi}\int_{A_0}\int_{A_0}\int_{-\frac{\pi}{\lambda_1}}^{\frac{\pi}{\lambda_1}}\int_{-\frac{\pi}{\lambda_2}}^{\frac{\pi}{\lambda_2}} \cdot\frac{cos[k_1\ (a_1-b_1)+k_2\ (a_2-b_2)][1-cos(k_1Ut)]}{k_1^2} \cdot\left(\delta_{1i}-\frac{k_1k_i}{k^2}\right)\left(\delta_{1j}-\frac{k_1k_j}{k^2}\right)\widehat{C}_Y(k_1,k_2)\ dk_1\ dk_2\ d^2\mathbf{a}\ d^2\mathbf{b}. \tag{29}$$

Let us now define the nonergodic dispersion tensor:

$$\widetilde{D}_{ij}^{eff}(t) = 0.5\frac{d\langle\widetilde{S}_{ij}(t)\rangle}{dt}. \tag{30}$$

[18] $\widetilde{D}_{ij}^{eff}$ is of limited value in applications, since nonergodic plumes are expected to show different patterns of evolution. Small plumes are affected significantly by local patterns of spatial variability, and are less amenable to description using dispersion coefficients. However, we can use this concept in order to determine the conditions under which $\widetilde{D}_{ij}^{eff} \rightarrow \widetilde{D}_{ij}^{ens}$. This is important because it will allow us to determine the conditions under which the plume becomes ergodic with respect to the subgrid variability, and hence is useful for grid design. Our analysis is focused on A_0 as representative of the plume's dimensions. Although in principle A_0 represents the plume's initial dimensions, we have established (see Figure 3) that the pre-asymptotic regime of $\widetilde{D}_{ij}^{ens}$ is relatively short, and hence A_0 can be viewed as generally representative of the plume's scales.

[19] Closed-form expressions for $\widetilde{D}_{11}^{eff}$ and $\widetilde{D}_{22}^{eff}$ for the case of an exponential covariance are provided in Appendix B, for $A_0 = l_1 \times l_2$, where l_1 and l_2 are in the x_1 and x_2 directions, respectively. Inspection of (28) and (29) reveals that $\widetilde{D}_{ij}^{eff}(t) \rightarrow 0$ as $\lambda_i \rightarrow 0$, since variations of all scales are reproduced on the grid. On the other hand as λ_i increases, $\widetilde{D}_{ij}^{eff}(t)$ approaches $D_{ij}^{eff}(t)$, because none of the hydraulic property variations are captured on the grid.

[20] Figure 5 shows the ratio between $\widetilde{D}_{11}^{eff,\infty}$ and $\widetilde{D}_{11}^{ens,\infty}$, the large-time asymptotic limits of $\widetilde{D}_{11}^{eff}$ and $\widetilde{D}_{11}^{ens}$, as a function of l_2 for various values of $\lambda = \lambda_1 = \lambda_2$. This diagram is useful for determining the conditions that warrant the use of $\widetilde{D}_{11}^{ens}$. If the difference is large, λ_i can be reduced, resulting in a larger value of l_2/λ_2, so that $\widetilde{D}_{11}^{eff,\infty}/\widetilde{D}_{11}^{ens,\infty}$ is close to its ergodic limit of 1. We have found that when the large-time asymptotic limits of the two coefficients are close, they are also close at early times. As l_2/λ_2 increases, $\widetilde{D}_{22}^{ens}$-$\widetilde{D}_{22}^{eff}$ declines to zero faster than $\widetilde{D}_{11}^{ens,\infty}$-$\widetilde{D}_{11}^{eff,\infty}$, such that when the use of $\widetilde{D}_{11}^{ens}$ is warranted, the use of $\widetilde{D}_{22}^{ens}$ is warranted, as well.

[21] Figure 5 shows that for l_2/λ>1.5, $\widetilde{D}_{11}^{ens,\infty}$ is very close to $\widetilde{D}_{11}^{eff,\infty}$ irrespective of λ/I_Y. For $l_2/\lambda = 1.5$ the relative difference between the two is less than 2.6%, for the exponential covariance model (Figure 5a) and 3.5% for the Gaussian covariance model (Figure 5b). This suggests that the plume becomes ergodic with respect to the wiped out variability when it is about 50% wider than λ. Under this condition, the effects of the subgrid variability can be modelled as Fickian dispersion. In other words, the wiped out variability can be accounted for using a dispersive flux, with the dispersion coefficient given by $\widetilde{D}_{ij}^{ens}$.

[22] Figure 6 extends Figure 5 to facilitate applications. It shows $l_2/I_{\widetilde{Y}}$ as a function of λ/I_Y for different l_2/I_Y ratios. It shows that the transverse dimension of the plume is generally quite large compared to the integral scale of the small-scale fluctuations. That partially explains the results shown in Figure 5. The shaded lines in Figure 6 correspond to $l_2/\lambda = 1.5$, which was found in Figure 5 to provide a safe definition of the ergodic limit. Thus the regions above the

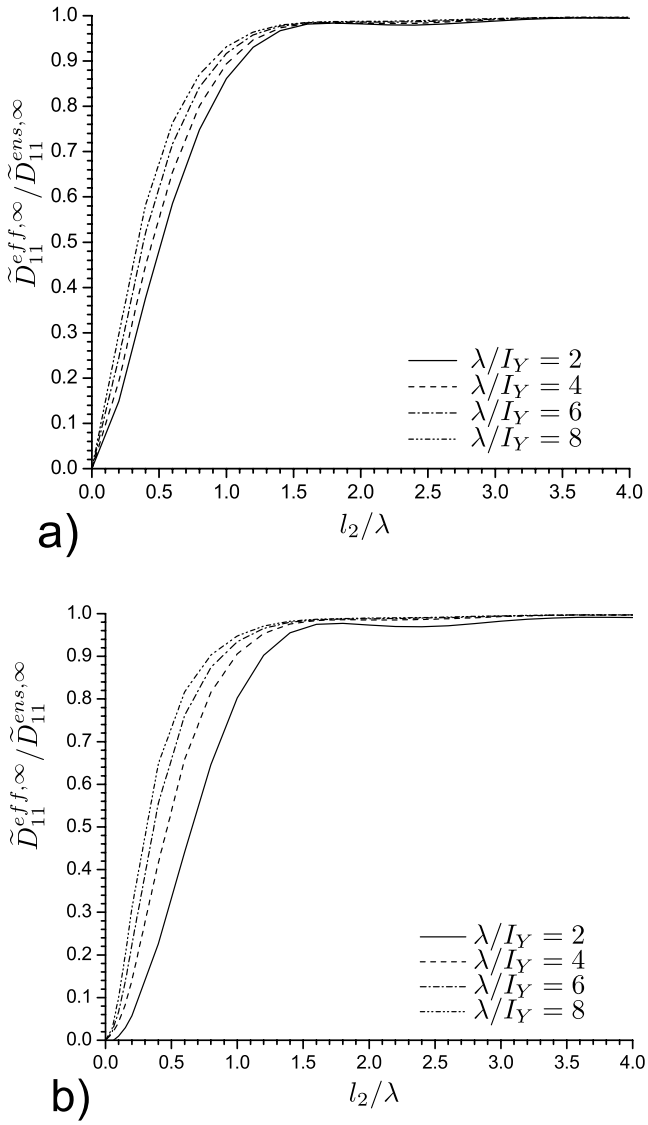

Figure 5. Ratio between the asymptotic large-time limits of the longitudinal effective, $\widetilde{D}_{11}^{eff}$, and ensemble average, $\widetilde{D}_{11}^{ens}$, block-scale macrodispersion coefficients versus l_2/λ for $l_1 \rightarrow 0$ and several values of $\lambda = \lambda_1 = \lambda_2$. (a) For the exponential isotropic covariance model (A1). (b) For the Gaussian isotropic model (11).

shaded lines define the range of scale where the $\widetilde{D}_{ij}^{ens}$ theory is applicable.

4. Numerical Testing

[23] In this section we report about numerical testing of $\widetilde{D}_{ij}^{ens}$. We will limit our test to cases where l_2 is sufficiently large compared to λ_2 to make the $\widetilde{D}_{ij}^{ens}$ concept applicable. The general plan is to simulate transport over a fine grid, such that spatial variability is captured in its entirety, followed by coarsening of the grid, and employing $\widetilde{D}_{ij}^{ens}$ to account for the lost variability. More specifically, our goal is to test our theory for $\lambda > \Delta$, and with that establish our ability to relax the link between the dimensions of homogenized regions and grid block dimensions.

[24] Numerical simulations are performed on planar flow in a heterogeneous domain characterized by an isotropic, exponential spatial covariance. The grid blocks are squares of dimension $\Delta \leq \lambda$. Unconditional realizations of the log conductivity fields are generated through HYDRO_GEN, the generator of correlated random functions developed by *Bellin and Rubin* [1996]. The domain is 48 I_Y long and 60 I_Y wide. Solute is released instantaneously over an area A_0 which is assumed rectangular with sides of length l_1 and l_2 in the longitudinal and transverse directions, respectively. Simulations are conducted with $l_1 = I_Y$ and several transverse dimensions, l_2, to simulate plumes of different sizes.

4.1. Fine-Grid Generation

[25] To make the numerical results for different values of λ insensitive to numerical errors introduced by the flow solver, in the first set of simulations the numerical grid spacing is set to $\Delta_1 = \Delta_2 = \Delta = 0.25\ I_Y$, following previously established standards [*Bellin et al.*, 1992; *Chin*, 1997]. Numerical experiments conducted by several authors [e.g., *Ababou et al.*, 1989; *Bellin et al.*, 1992; *Chin*, 1997] have shown that higher wave numbers have a negligible dispersive effect. This is also confirmed by the fact that for $\lambda = 0.25\ I_Y$, the asymptotic large-time limit of the effective block-scale macrodispersion coefficient, $\widetilde{D}_{11}^{eff,\infty}/(U\ I_Y\ \sigma_Y^2)$ (B5), is equal to 0.003, a value much smaller than $D_{11}^{*}(t \rightarrow \infty)$, (equation (9)).

[26] The log-hydraulic conductivity is generated at the center of the numerical grid blocks, and the flow solver is based on Galerkin's finite element scheme with triangular elements obtained by splitting the square in two parts. The particle-tracking methodology to solve for transport is discussed in Appendix C.

4.2. Fine-Grid Results

[27] Figure 7 compares numerical and analytical results for the expected value of the longitudinal spatial moments $\langle S_{11} \rangle$ (see equation (22)) for several values of λ as a

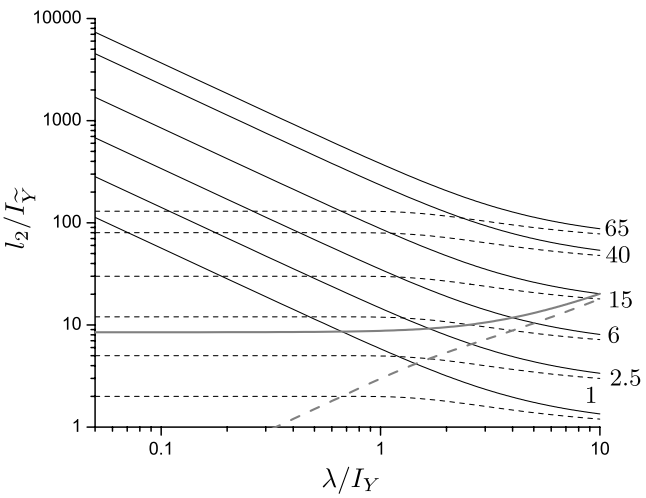

Figure 6. $l_2/I_{\widetilde{Y}}$ as a function of λ/I_Y for several values of l_2/I_Y (marked on the curves) for the exponential isotropic covariance (A1) (solid line), and the Gaussian isotropic covariance (11) (dashed line). The shaded lines correspond to $l_2/\lambda = 1.5$. The regions above the lines can be assumed to safely satisfy the ergodic limit $\widetilde{D}_{11}^{ens} = \widetilde{D}_{11}^{eff}$.

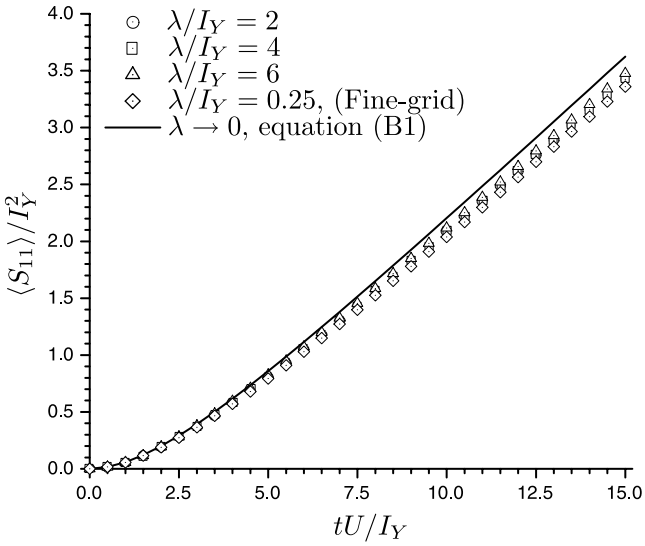

Figure 7. Unconditional $\langle S_{11}\rangle$ for different λ for a transverse source size of $l_2/I_Y = 10$. Diamonds indicate the moments obtained with the fine-grid simulation. The other symbols indicate numerical moments obtained by performing transport experiments on large-scale velocity fields and accounting for unresolved small-scale variability with the ensemble average block-scale macrodispersion. The first-order solution for $\langle S_{11}\rangle$, (B1), is indicated with a solid line. In all cases $\sigma_Y^2 = 0.2$, $\lambda_1 = \lambda_2 = \lambda$, and $\Delta = 0.25\ I_Y$.

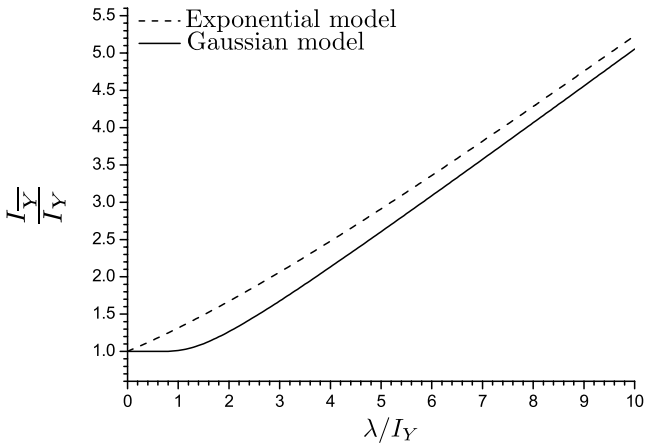

Figure 8. The ratio of the integral scale of $\overline{Y}$ to that of Y as a function of λ for both exponential (A1) and Gaussian (11) spatial correlations of hydraulic conductivity with $I_{Y,1} = I_{Y,2} = I_Y$ and $\lambda_1 = \lambda_2 = \lambda$.

function of time. The grid blocks are fixed at $\Delta = 0.25\ I_Y$, irrespective of λ. The results are for $\sigma_Y^2 = 0.2$ and $l_2 = 10\ I_Y$. Unresolved small-scale variability is modeled through $\widetilde{D}_{ii}^{ens}$ (equations (42) and (43) of *Rubin et al.* [1999]), since, as shown in Figure 5, the smallest l_2/λ, which is equal to 1.7, is large enough such that $\widetilde{D}_{11}^{eff}$ is close to $\widetilde{D}_{11}^{ens}$. These large λ results resemble both the analytical solution and the numerical fine-grid solution, with differences that increase with λ, but do not exceed 3.5% for the unrealistically high $\lambda = 6\ I_Y$ at large times. For $\sigma_Y^2 = 1$ these differences are 5.2, 7.4 and 5 times larger than with $\sigma_Y^2 = 0.2$, for $\lambda/I_Y = 2$, 4 and 6, respectively, suggesting a linear increase of the difference with σ_Y^2. These differences are due to the inability of $\widetilde{D}_{ii}^{ens}$ to capture higher-order terms at scales smaller than λ, and the assumed independence of small- and large-scale fluctuations in (4), whose effects are accounted for in the fine-grid simulation.

4.3. Effect of Grid Block Size on Numerical Error

[28] Our previous discussion focused on the $\widetilde{D}_{ij}^{ens}$ concept and on its ability to compensate for the wiped out variability. In particular we establish the order relationship between l_2 and λ_2 (see Figure 1) needed to secure its applicability. The issue we raise now is how much we can increase Δ while maintaining the applicability of $\widetilde{D}_{ij}^{ens}$. In this regard, one should be concerned about being able to capture $\widehat{C}_{\overline{Y}}(\boldsymbol{k})$ accurately. Our discussion is motivated by noting that $\widehat{C}_{\overline{Y}}(\boldsymbol{k})$ is characterized by $I_{\overline{Y}} > I_Y$. It is common to employ a grid block scale which is of the order of $\sim 0.25\ I_Y$, and hence with $I_{\overline{Y}} > I_Y$, there is some latitude to work with large Δ. This effect is demonstrated in Figure 8, which shows the increase of $I_{\overline{Y}}$ corresponding to the increase in λ. Figure 9 compares the average longitudinal moments of S_{11} corresponding to different λ values and a fixed l_2. We maintained a constant ratio $\Delta/I_{\overline{Y}} = 0.25$ (this obviously translates to different Δ/I_Y ratios, as shown in Figure 9, as can be verified with the aid of Figure 8).

[29] Figure 9 shows the relative difference between $\langle S_{11}\rangle$ computed with different λ as shown and $\Delta = 0.25\ I_{\overline{Y}}$, and $\langle S_{11}\rangle$ computed using fine grid $\Delta = 0.25\ I_Y$ and $\lambda \to 0$. The relative difference shown in Figure 9 is $\Delta S_{11}(t) = [\langle S_{11}\ (t, \Delta = 0.25\ I_{\overline{Y}}, \lambda)\rangle - \langle\ S_{11}(t, \Delta = 0.25\ I_Y, \lambda \to 0)\ \rangle]/\langle S_{11}(t, \Delta = 0.25\ I_Y, \lambda \to 0)\rangle$. We note that in the range of values investigated, ΔS_{11} is rather small: for $tU/I_Y > 0.25$, its maximum values are 4.7%, 7.6%, and 9.9% for $\lambda/I_Y = 2$, 4 and 6, respectively. To separate errors associated with $\widetilde{D}_{ij}^{ens}$ from numerical error due to large Δ, we repeated the analysis with the moments shown in Figure 7, which are obtained by using the same refined grid with $\Delta = 0.25\ I_Y$,

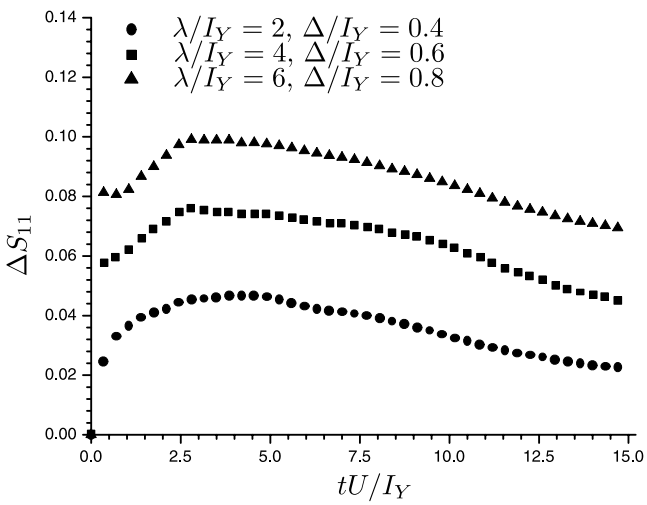

Figure 9. Relative difference, ΔS_{11}, for several block sizes and values of λ. Numerical simulations are performed choosing Δ in such a way as to maintain constant the ratio between Δ and $I_{\overline{Y}}$, the integral scale of the large-scale spatial variability. In all cases $\lambda_1 = \lambda_2 = \lambda$, $\Delta_1 = \Delta_2 = \Delta$, $\sigma_Y^2 = 0.2$ and $l_2 = 10\ I_Y$.

irrespective of λ. The resulting ΔS_{11} are smaller than in the previous case. Specifically, the maximum values of ΔS_{11} for λ/I_Y = 2, 4 and 6 are 2.5%, 2.7%, and 4.1%, respectively. The portion of the differences shown in Figure 9 exceeding these values are the consequence of numerical error, which for Galerkin's flow solver is proportional to the grid size, and should not be attributed to our method. We conclude that for small λ the numerical grid can be designed with the aid of Figure 8 such as to respect the condition $\Delta = 0.25 I_{\overline{Y}}$, while for large λ a smaller grid size is needed to limit numerical error of the flow solver, and inspection of Figure 8 with $I_{\overline{Y}} = 4\Delta$ provides the value of λ corresponding to the selected Δ.

5. Summary and Conclusions

[30] This paper develops and tests a theory for modeling the effects of subgrid-scale variability on solute mixing, using block-effective macrodispersion coefficients, following ideas presented by *Rubin et al.* [1999]. The fundamental question we consider in this paper is how to allow flexibility in numerical grid design, on the one hand, without discounting the dispersive action of the unmodeled variability, on the other. Our approach allows analysis of grid spacing and elimination of unnecessary high grid density. It is formally applicable to mild heterogeneity, $\sigma_Y^2 \leq 1$. The block-effective macrodispersion coefficients depend, in general, on the grid-scale and the plume scale, and they are derived based on Nyquist's theorem which allows separation between the length scales which affect mixing and those which affect advection. When the ratio between the plume's lateral dimensions and the block's scales exceeds ~1.5, the dependence on the plume's scale vanishes. When this ratio is met, the plume is ergodic with regard to the integral scale of the wiped out, subgrid-scale heterogeneity, and the block-effective coefficients can in fact be considered as deterministic descriptors of the effects of the wiped out variability on mixing.

[31] Unlike the case of macrodispersion coefficients, the block effective ones reach their asymptotic limit quite early, for typical plume and grid scales. This implies that in cases where the block effective macrodispersion coefficients are applicable, they are uniform, provided that blocks of equal dimensions are employed. However, it is reasonable to expect that the numerical grids be designed adaptively [cf. *Durlofsky et al.*, 1997], which allows variable λ_i and Δ_i. In this case, grid blocks of similar dimensions will be characterized by different $\widetilde{D}_{ij}^{ens}$, depending on the dimensions of the homogenized regions. Our method allows a systematic analysis of the relationships between the numerical grid block's dimensions Δ_i (i = 1,.., m) and the dimensions of uniform regions λ_i. In applications, this relationship can be used in different ways. The first is to select Δ_i given λ_i. Alternatively, it can be used to select λ_i for given Δ_i, when Δ_i are determined such as to minimize numerical error, or to limit the computational burden. In both cases the plume's scales l_i need to be considered as well. For example, following Figure 5, we note that in planar flow situations we should adhere to a ratio $l_2/\lambda > 1.5$, in order to be able to model effectively the effects of the wiped out variability using $\widetilde{D}_{ij}^{ens}$. Once the appropriate λ is selected, values for $\widetilde{D}_{ij}^{ens}$ can be determined using Figure 3 or equation (10). Closed form solutions for planar flow for the Gaussian and exponential covariance models of Y are provided as well.

Appendix A: Variance and Integral Scale of the Large-Scale Variability

[32] Let us consider first the two-dimensional exponential isotropic covariance model

$$C_Y(r_1, r_2) = \sigma_Y^2 \, e^{-r'}; \quad r' = \sqrt{\frac{r_1^2 + r_2^2}{I_Y^2}} \tag{A1}$$

with the following power spectrum:

$$\widehat{C}_Y(k_1, k_2) = \frac{\sigma_Y^2 \, I_Y^2}{[1 + (k_1^2 + k_2^2) I_Y^2]^{3/2}}. \tag{A2}$$

Substituting (A2) into (8), and assuming $\lambda_1 = \lambda_2 = \lambda$, we obtain after integration:

$$\sigma_{\overline{Y}}^2 = \frac{2}{\pi} \cot^{-1}\left(\frac{\lambda}{\pi^2 I_Y^2} \sqrt{2\pi 7^2 I_Y^2 + \lambda^2}\right) \sigma_Y^2. \tag{A3}$$

[33] The integral scale of $\overline{Y}$ along the direction x_1 is obtained by substituting (7) into (20), and integrating:

$$I_{\overline{Y},1} = \frac{\pi^2 I_Y^2}{2\sqrt{\pi^2 I_Y^2 + \lambda^2} \; cot^{-1}\left[\frac{\lambda}{I_Y^2 \pi^2} \sqrt{2\pi^2 I_Y^2 + \lambda^2}\right]} \tag{A4}$$

[34] The corresponding expressions for the isotropic Gaussian covariance model, which is obtained from (11) assuming $I_{Y,1} = I_{Y,2}$, are as follows:

$$\sigma_{\overline{Y}}^2 = erf\left[\frac{\sqrt{\pi} \, I_Y}{\lambda}\right]^2 \sigma_Y^2 \tag{A5}$$

and

$$I_{\overline{Y},1} = erf\left[\frac{\sqrt{\pi} \, I_Y}{\lambda}\right]^{-1} I_Y. \tag{A6}$$

Appendix B: Effective Small- and Large-Scale Plume Moments and Macrodispersion Coefficients

[35] We consider here a two-dimensional aquifer with constant thickness and spatial correlation of the hydraulic conductivity described by the model (A1). For an instantaneous release of solute with constant concentration, C_0, within the volume, V_0, extending over the entire thickness, b, of the aquifer and with rectangular horizontal projection $A_0 = l_1 \times l_2$ centered at the origin of the coordinate system, the effective longitudinal second-order moment is given by

$$\langle S_{11}(t) \rangle = S_{11}(0) + X_{11}(t) - \frac{64 \, \sigma_Y^2 I_Y^2}{l_1'^2 \, l_2'^2 \, \pi} \int_0^\infty \int_0^\infty \frac{k_2'^2 \left[1 - \cos(k_1' t')\right] \sin^2\left[\frac{k_2' l_2'}{2}\right] \sin^2\left[\frac{k_1' l_1'}{2}\right]}{k_1'^4 \left[k_1'^2 + k_2'^2\right]^2 \left[1 + k_1'^2 + k_2'^2\right]^{\frac{3}{2}}} \, dk_2' \, dk_1' \tag{B1}$$

where X_{11} is the longitudinal particle displacement variance obtained by *Dagan* [1984] and is reproduced here for convenience:

$$\frac{X_{11}(t)}{\sigma_Y^2 I_Y^2} = -0.231647 + 2t' + 3\left[\frac{(1+t')\,e^{-t'}-1}{t'^2} + Ei(-t')\right] - 3\,\ln(t'). \tag{B2}$$

Here and throughout Appendix B, $t' = tU/I_Y$ is the dimensionless time, $l_i' = l_i/I_Y$, and $k_i' = k_i I_Y$, $i = 1, 2$.

[36] Similarly, the large-scale effective longitudinal second-order moment assumes the following form

$$\langle \overline{S}_{11}(t)\rangle = \overline{X}_{11}(t) - \frac{64\,\sigma_Y^2 I_Y^2}{l_1'^2\, l_2'^2\,\pi}\int_0^{\frac{\pi}{\lambda_1'}}\int_0^{\frac{\pi}{\lambda_2'}} \cdot \frac{k_2'^2\left[1-\cos(k_1' t')\right]\sin\left[\frac{k_2' l_2'}{2}\right]^2 \sin\left[\frac{k_1' l_1'}{2}\right]^2}{k_1'^4\left[k_1'^2+k_2'^2\right]^2\left[1+k_1'^2+k_2'^2\right]^{\frac{3}{2}}}\,dk_2'\,dk_1', \tag{B3}$$

where

$$\overline{X}_{11}(t) = 2\,\sigma_Y^2\, I_Y^2 \int_0^{\frac{\pi}{\lambda_1'}} \left\{ \frac{\left(2+3k_1'^2\right)\pi^2 + 3k_1'^2\left(1+k_1'^2\right)\lambda_2'^2}{k_1'\sqrt{1+k_1'^2+\frac{\pi^2}{\lambda_2'^2}}\,\lambda_2'\left(\pi^2+k_1'^2\lambda_2'^2\right)} - \frac{3}{\pi}\left(1+k_1'^2\right) cot^{-1}\left[\frac{k_1'}{\pi}\sqrt{1+k_1'^2+\left(\frac{\pi}{\lambda_2'}\right)^2}\,\lambda_2'\right] \right\} \cdot \frac{\left(1-\cos(k_1' t')\right)}{k_1'}\,dk_1' \tag{B4}$$

is the large-scale component of the variance of the particle displacement. It represents the spreading of an ergodic plume in the two-dimensional large-scale log conductivity field $\overline{Y}$. In (B3) and (B4), $\lambda_i' = \lambda_i/I_Y$, for $i = 1, 2$.

[37] The effective longitudinal small-scale macrodispersion coefficient, $\widetilde{D}_{11}^{eff}$, assumes the following form

$$\widetilde{D}_{11}^{eff}(t) = \frac{1}{2}\left[\frac{d}{dt}\langle S_{11}(t)\rangle - \frac{d}{dt}\langle \overline{S}_{11}(t)\rangle\right] = D_{11}^{eff}(t) - \overline{D}_{11}^{eff}(t), \tag{B5}$$

where

$$D_{11}^{eff}(t) = D_{11}^{*}(t) - \frac{32\,\sigma_Y^2\, U\, I_Y}{l_1'^2\, l_2'^2\,\pi}\int_0^{\infty}\int_0^{\infty} \frac{k_2'^2 \sin\left(\frac{k_2' l_2'}{2}\right)^2 \sin\left(\frac{k_1' l_1'}{2}\right)^2 \sin(k_1' t')}{k_1'^3\left(k_1'^2+k_2'^2\right)^2\left(1+k_1'^2+k_2'^2\right)^{\frac{3}{2}}}\,dk_2'\,dk_1', \tag{B6}$$

with D_{11}^{*}representing the longitudinal dispersion coefficient of an ergodic plume [*Dagan*, 1984]

$$\frac{D_{11}^{*}(t)}{\sigma_Y^2\, U\, I_Y} = \frac{-6\,(1+t') + \exp(t')\left[6+t'^2\,(-3+2t')\right]}{2\,\exp(t')\,t'^3}. \tag{B7}$$

[38] Similarly, the longitudinal large-scale effective dispersion coefficient assumes the following form

$$\overline{D}_{11}^{eff}(t) = \overline{D}_{11}^{ens}(t) - \frac{32\,\sigma_Y^2\, U\, I_Y}{l_1'^2\, l_2'^2\,\pi}\int_0^{\frac{\pi}{\lambda_1'}}\int_0^{\frac{\pi}{\lambda_2'}} \frac{k_2'^2 \sin\left(\frac{k_2' l_2'}{2}\right)^2 \sin\left(\frac{k_1' l_1'}{2}\right)^2 \sin(k_1' t')}{k_1'^3\left(k_1'^2+k_2'^2\right)^2\left(1+k_1'^2+k_2'^2\right)^{\frac{3}{2}}}\,dk_2'\,dk_1', \tag{B8}$$

where the longitudinal large-scale ergodic dispersion coefficient is given by

$$\frac{\overline{D}_{11}^{ens}(t)}{\sigma_Y^2\, U\, I_Y} = \int_0^{\frac{\pi}{\lambda_1'}} \left[\frac{\left(2+3k_1'^2\right)\pi^2 + 3k_1'^2\left(1+k_1'^2\right)\lambda_2'^2}{k_1'\sqrt{1+k_1'^2+\frac{\pi^2}{\lambda_2'^2}}\,\lambda_2'\left(\pi^2+k_1'^2\lambda_2'^2\right)} - \frac{3}{\pi}\left(1+k_1'^2\right)\cot^{-1}\left(\frac{k_1'}{\pi}\sqrt{1+k_1'^2+\frac{\pi^2}{\lambda_2'^2}}\;\lambda_2'\right) \right] \cdot \sin(k_1' t')\,dk_1'. \tag{B9}$$

[39] Similar expressions can be obtained in the transverse direction:

$$\widetilde{D}_{22}^{eff}(t) = D_{22}^{eff} - \overline{D}_{22}^{eff}, \tag{B10}$$

where

$$D_{22}^{eff}(t) = D_{22}^{*}(t) - \frac{32\,\sigma_Y^2\, U\, I_Y}{l_1'^2\, l_2'^2\,\pi}\int_0^{\infty}\int_0^{\infty} \cdot \frac{\sin\left(\frac{k_1' l_1'}{2}\right)^2 \sin\left(\frac{k_2' l_2'}{2}\right)^2 \sin(k_1' t')}{k_1'\left(k_1'^2+k_2'^2\right)^2\left(1+k_1'^2+k_2'^2\right)^{\frac{3}{2}}}\,dk_2'\,dk_1', \tag{B11}$$

with

$$\frac{D_{22}^{*}(t)}{\sigma_Y^2 U I_Y} = \frac{e^{t'}\left(-6+t'^2\right)+2\,(3+t'\,(3+t'))}{2\,e^{t'}\,t'^3}. \tag{B12}$$

Furthermore, the large-scale effective transverse macrodispersion coefficient is given by

$$\overline{D}_{22}^{eff} = \overline{D}_{22}^{ens}(t) - \frac{32\,\sigma_Y^2\, U\, I_Y}{l_1'^2\, l_2'^2\,\pi}\int_0^{\frac{\pi}{\lambda_1'}}\int_0^{\frac{\pi}{\lambda_2'}} \cdot \frac{\sin\left(\frac{k_1' l_1'}{2}\right)^2 \sin\left(\frac{k_2' l_2'}{2}\right)^2 \sin(k_1' t')}{k_1'\left(k_1'^2+k_2'^2\right)^2\left(1+k_1'^2+k_2'^2\right)^{\frac{3}{2}}}\,dk_2'\,dk_1', \tag{B13}$$

with

$$\frac{\overline{D}_{22}^{ens}(t)}{\sigma_Y^2\, U\, I_Y} = \int_0^{\frac{\pi}{\lambda_1'}} \left[\frac{\left(1+3k_1'^2\right)}{\pi}\cot^{-1}\left(\frac{k_1'\lambda_2'}{\pi}\sqrt{1+k_1'^2+\frac{\pi^2}{\lambda_2'^2}}\right) - \left(\frac{k_1'\left(3\pi^2+\left(1+3k_1'^2\right)\lambda_2'^2\right)}{\lambda_2'\sqrt{1+k_1'^2+\frac{\pi^2}{\lambda_2'^2}}\left(\pi^2+k_1'^2\lambda_2'^2\right)}\right) \right] \sin(k_1' t')\,dk_1'. \tag{B14}$$

Appendix C: Particle-Tracking Methodology

[40] Following the Lagrangian approach, the total mass per unit of thickness, $m_0 = M_0/b = n\,C_0 A_0$, of solute with

constant concentration, C_0, released instantaneously within the volume $V_0 = A_0 b$, where b is the thickness of the formation, is split into a large number, NP, of noninteracting particles. Each particle is tracked according to the following scheme:

$$X^{\nu}_{p,i}(t) = X^{\nu}_{p,i}(t-\Delta t) + \overline{u}^{\nu}_i(\mathbf{X}^{\nu}_p(t-\Delta t))\Delta t + \Delta X^{\nu}_{B;p,i}(t), \quad \text{(C1)}$$

where $X^{\nu}_{p,i}$, $i = 1,2$ is the i-th component of the trajectory of the particle p in the realization ν of the log conductivity field, $\overline{u}_i{}^{\nu}$ is the i^{th} component of the large-scale velocity field obtained numerically by solving the flow equation, Δt is the time step, and $\Delta X^{\nu}_{B;p,i}$ is the i-th component of the Brownian motion introduced to model block dispersivity and pore-scale dispersion, if present,

$$\Delta X^{\nu}_{B;p,i}(t) = \epsilon^{\nu}_{p,i}\sqrt{2\left[\tilde{D}^{ens}_{ii}(t) + D_{d,i}\right]\Delta t}. \quad \text{(C2)}$$

In (C2), $D_{d,i}$ is the pore-scale dispersion tensor and $\epsilon^{\nu}_{p,i}$ is a random variable normally distributed with zero mean and unit variance. Furthermore, Δt is chosen such that both $\Delta\overline{\mathbf{X}}^{\nu}_{B;p}$ and $\Delta\mathbf{X}^{\nu} = \mathbf{U}^{\nu}(\mathbf{X}^{\nu}_p(t\text{-}\Delta t))\,\Delta t$ are much smaller than the grid block size. In our simulations, this is accomplished with $\Delta t/(U\,I_Y) = 0.05$ and 0.01 for $\sigma_Y{}^2 = 0.2$ and $\sigma_Y{}^2 = 1$, respectively. Initial spacing between the particles is $0.05\,I_Y$ in both the longitudinal and transverse directions. Pore-scale dispersion is neglected in our simulations.

[41] The spatial moments are computed as follows

$$R^{\nu}_i(t) = \frac{1}{NP}\sum_{p=1}^{NP} X^{\nu}_{p,i}(t),$$

$$S^{\nu}_{ij}(t) = \frac{1}{NP}\sum_{p=1}^{NP}\left[X^{\nu}_{p,i}(t) - R^{\nu}_i(t)\right]\left[X^{\nu}_{p,j}(t) - R^{\nu}_j(t)\right]. \quad \text{(C3)}$$

To obtain a representative sample of the statistical population of all possible plume moments, the transport experiment is repeated in MC independent Monte Carlo realizations of the log conductivity field. The statistics of the plume moments

$$\langle R_i(t)\rangle = \frac{1}{MC}\sum_{\nu=1}^{MC} R^{\nu}_i(t), \langle S_{ij}(t)\rangle = \frac{1}{MC}\sum_{\nu=1}^{MC} S^{\nu}_{ij}(t), \quad \text{(C4)}$$

$$R_{ij}(t) = \frac{1}{MC}\sum_{\nu=1}^{MC}\left[R^{\nu}_i(t) - \langle R_i(t)\rangle\right]\left[R^{\nu}_j(t) - \langle R_j(t)\rangle\right],$$

$$var[S_{ij}(t)] = \frac{1}{MC}\sum_{\nu=1}^{MC}\left[S^{\nu}_{ij}(t) - \langle S_{ij}(t)\rangle\right]^2 \quad \text{(C5)}$$

are then computed. The ergodic second-order moments X_{ij} are computed by substituting the moments $\langle S_{ij}\rangle$ and R_{ij} obtained by (C4) and (C5) into (24). The number of Monte Carlo realizations is chosen to control the convergence of $var[S_{ij}]$, the highest order moment considered, as suggested by *Bellin et al.* [1992].

References

Ababou, R. D., D. McLaughlin, L. W. Gelhar, and A. F. B. Tompson, Numerical simulation of three-dimensional saturated flow in randomly heterogeneous porous media, *Transp. Porous Media*, *4*, 549–565, 1989.

Bellin, A., and Y. Rubin, HYDRO_GEN: A spatially distributed random field generator for correlated properties, *Stochastic Hydrol. Hydraul.*, *10*, 253–278, 1996.

Bellin, A., P. Salandin, and A. Rinaldo, Simulation of dispersion in heterogeneous porous formations: Statistics, first-order theories, convergence of computations, *Water Resour. Res.*, *28*, 2211–2227, 1992.

Bras, R. L., and I. Rodriguez-Iturbe, *Random Functions and Hydrology*, Addison-Wesley-Longman, Reading, Mass., 1985.

Chin, D. A., An assessment of first-order stochastic dispersion theories in porous media, *J. Hydrol.*, *199*, 53–73, 1997.

Dagan, G., Solute transport in heterogeneous porous formations, *J. Fluid Mech.*, *145*, 151–177, 1984.

Dagan, G., *Flow and Transport in Porous Formations*, Springer-Verlag, New York, 1989.

Dagan, G., Dispersion of a passive solute in non-ergodic transport by steady velocity fields in heterogeneous formations, *J. Fluid Mech.*, *223*, 197–210, 1991.

Durlofsky, L. J., R. C. Jones, and W. J. Milliken, A non-uniform coarsening approach for the scale-up of displacement processes in heterogeneous porous media, *Adv. Water Res.*, *20*, 335–347, 1997.

Kitanidis, P. K., Prediction by the method of moments of transport in heterogeneous formation, *J. Hydrol.*, *102*, 453–473, 1988.

Rubin, Y., *Applied Stochastic Hydrogeology*, Oxford Univ. Press, New York, 2003.

Rubin, Y., and A. Bellin, The effects of recharge on flow nonuniformity and macrodispersion, *Water Resour. Res.*, *30*, 939–948, 1994.

Rubin, Y., A. Sun, R. Maxwell, and A. Bellin, The concept of block-effective macrodispersivity and a unified approach for grid-scale- and plume-scale-dependent transport, *J. Fluid Mech.*, *395*, 161–180, 1999.

Wang, J., and P. K. Kitanidis, Analysis of macrodispersion through volume averaging: Comparison with stochastic theory, *Stochastic Environ. Res. Risk Assess.*, *13*, 66–84, 1999.

A. Bellin, Dipartimento di Ingegneria Civile ed Ambientale, Università di Trento, via Mesiano 77, I-38050 Trento, Italy. (alberto.bellin@ing.unitn.it)

A. E. Lawrence and Y. Rubin, Department of Civil and Environmental Engineering, University of California at Berkeley, 435 Davis Hall, Berkeley, CA 94720, USA. (lawrence@ce.berkeley.edu; rubin@ce.berkeley.edu)